ELSEVIER

Journal of Crystal Growth 181 (1997) 133–144

JOURNAL OF CRYSTAL GROWTH

Segregation during horizontal Bridgman growth under an axial magnetic field

T. Alboussière[1,a], A.C. Neubrand[b], J.P. Garandet[b,*], R. Moreau[a]

[a] *Laboratoire EPM-Madylam, CNRS UPR A 9033, ENSHMG, BP 95, F-38402 St. Martin d'Hères Cedex, France*

[b] *Commissariat à l'Énergie Atomique, DTA/CEREM/DEM/LRBS, Centre d'Études Nucléaires de Grenoble, 17 avenue des Martyrs, F-38054 Grenoble Cedex 09, France*

Received 11 April 1997; accepted 11 April 1997

Abstract

Solute segregation in a dilute metallic alloy is investigated during horizontal Bridgman growth. Experiments have been carried out under a permanent uniform axial magnetic field of intensity up to 1.35 T. The field is seen to have a moderate effect on axial segregation. A 2D model for segregation is presented and solved both numerically and in terms of order of magnitude analysis. Accounting for the measurement errors and the 2D nature of the analysis, a good agreement is obtained with the experimental results. The theoretical analyses exhibit a critical value for the magnetic field intensity. Below, the magnetic field has no effect on solute segregation, while above, the effective partition ratio is increasing with increasing magnetic field intensity.

Keywords: Dopant segregation; Bridgman method; Mass transport; Magnetohydrodynamics; Experiments; Order of magnitude analysis

1. Introduction

It is well known that a permanent magnetic field has the effect of reducing the strength of thermogravitational convection in metal melts during solidification. In that respect, magnetic damping and microgravity are two interesting possibilities for reducing fluid velocity in an experiment. In crystal growth, an optimal compositional homogeneity in the resulting solid is observed under diffusive solute transport conditions. Such a result is interesting for doped semi-conductors since they are electrically conducting in the liquid phase and since a high homogeneity is required for electronic or opto-electronic applications. Some studies already report the effectiveness of a steady magnetic field. Hurle et al. [1] use a steady magnetic field to

* Corresponding author. Fax: + 33 476 885117.

[1] Present address: Engineering Department, Cambridge University, Trumpington Street, Cambridge CB2 1PZ, UK.

PII S0022-0248(97)00275-3

stabilize turbulence and hence to eliminate striations, Vives and Perry [2] study the magnetic damping effect on convection during solidification while Matthiesen et al. [3] show experimentally a reduction of the axial segregation, with a strong axial magnetic field during vertical Bridgman growth.

The purpose of this paper is to quantify and model the influence of an axial uniform magnetic field on segregation during alloy solidification in the horizontal Bridgman method. We performed experimental metallic alloy solidifications under different magnetic field intensities and the results are reported here in terms of the effective partition ratio deduced from concentration measurements in the resulting solid. In parallel, we propose a coupled order of magnitude analysis /numerical modelling of the transport phenomena in the melt. To do so, we first study the thermogravitational motion under a magnetic field in the horizontal Bridgman configuration and then focus on the effect of such a flow on segregation. Our model is limited to the dilute alloys to avoid studying the coupling effect of concentration on buoyancy.

Section 2 is devoted to a presentation of our experimental work in terms of growth conditions and results. In Section 3 the MHD liquid flow is analyzed and an order of magnitude analysis is built to estimate segregation. Direct numerical simulations of segregation are also carried out. Finally, the results of these analyses are compared with the experiments.

2. Experimental procedure

2.1. BRAHMS

An experimental device, called BRAHMS (Bridgman related apparatus for hydrodynamic and magnetic studies) was designed for the purpose of horizontal Bridgman growth under an axial magnetic field (see Fig. 1). In our experiments, a metallic alloy Sn–Bi (0.13 or 0.05 at.% Bi) was chosen. This low composition allows us to neglect any solute buoyancy effect, as will be shown in Section 3.1, and also postpones growth interface destabilization. The diameter of the sample was 6 mm – the sample itself being contained in a quartz crucible ($\phi_{int} = 6$ mm, $\phi_{ext} = 10$ mm) – while the directionally solidified length reached 20 cm. Well-controlled experimental conditions were specified: the value of the axial temperature gradient is 24 K cm^{-1} in the melt with uniformity better than 5% from the interface to 12 cm further. The Bitter coil produces a maximum magnetic field

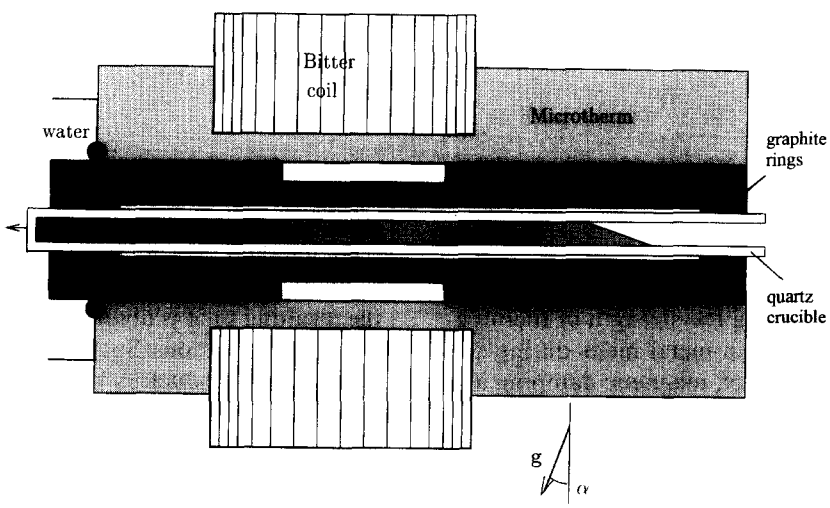

Fig. 1. General view of BRAHMS.

magnitude of 1.35 T; the intensity variation is less than 10% from the interface to 8 cm apart. The crucible and sample were pulled by a step by step motor: each step corresponds to a 0.1 μm axial displacement, and is itself divided in ten, possibly unequal,"micro-steps". The investigated pulling rates range from 2.5 μm s^{-1} to 10 μm s^{-1}.

The thermal principle of BRAHMS is simple and efficient in producing an almost purely axial temperature gradient. The key point is that the sample and crucible are surrounded by a silver tube. Silver has the highest thermal conductivity among metals: 400 W m^{-1} K^{-1} in our working temperature range. Indeed, for a given axial thermal gradient, the axial heat flux is drastically enhanced and makes thus negligible the radial heat losses (which only depend on the insulating material and temperature difference between the external air and the tube). As a result, the temperature gradient is almost axial in the silver. Nevertheless, the question remains of radial heat exchanges between the sample and the silver tube: these exchanges have to be minimized to achieve an axial thermal gradient in the sample. When these exchanges are zero, the axial heat flux in the sample is constant along the axis, since convection heat transport can safely be neglected in liquid tin, that has a Prandtl number of 0.013. Conservation of the heat flux at the interface implies that the axial temperature gradient is twice higher in the liquid than in the solid since the ratio of the thermal conductivity of solid to that of liquid tin is about two. Conversely, if the axial heat conductance of the silver tube mimics that of the sample, no radial heat exchanges will develop. This condition is achieved when the silver cross-section ratio is two between the solid and the liquid sample region (see Fig. 1). The axial temperature gradient (24 K cm^{-1}) is created by heating wires in the hot part, with a 600°C temperature regulation (Eurotherm 818P4) and by a cold water flow in the other side (regulation: $T_{water} = 20°C$). A micro-porous insulating material (Microtherm) has been used outside the silver tube. It has a very low thermal conductivity, from 0.015 W m^{-1} K^{-1} at 20°C to 0.03 W m^{-1} K^{-1} at 500°C.

The thermal core of BRAHMS (the silver tube with its insulating material) has a 50 mm diameter. The smaller this diameter is, the higher can be the magnetic field intensity generated by the coil. In a Bitter coil, instead of winding a wire, the electric circuit is made of a pile of copper annular disks separated by thin electrically insulating Kapton disks. A small sector is cut off in each copper disk while a 20° sector is cut off in each Kapton disk. The electrical current path is controlled by imposing a 20° angular rotation from one copper disk to another, the contact being made through the cut-off sector of the Kapton disk. In order to improve the magnetic field uniformity, the current density can be adjusted by grouping some copper disks in parallel near the ends of the coil. As shown in Fig. 1, this was done in our experimental device. All the disks contain a large number of holes (about 300, $\phi = 1.25$ mm), precisely aligned and forming ducts, where the cooling water can flow. The exchange surface between water and copper is very large, and the pressure loss minimized. From an electrical point of view, a Bitter coil is an optimum solution: first the copper volume fraction is more than 90%, and second the induced 1/r current density distribution renders maximum the ratio of the magnetic field intensity to the electric power needed. We obtain 1.35 T with 90 kW.

Its orientability with respect to gravity is another feature of BRAHMS. As our crucibles were open at the hot side, a 15° angle with the horizontal had to be maintained to prevent molten tin to flow out of the crucible. In fact, as the temperature gradient is almost axial, the buoyant driving force is proportional to the part of gravity orthogonal to the axis (otherwise stated, only the curl of the buoyant force density produces motion).This has been used to simulate a smaller gravity, by varying the inclination of BRAHMS ($\alpha = 15°$, 60° and 75°, see Fig. 1).

2.2. Experimental results

The results of our experiments are related to the axial solute segregation in the solidified sample. This axial segregation is expressed classically as an effective partition ratio k^* (see, Ref. [4]). This effective partition ratio ranges from one for purely diffusive conditions to the equilibrium partition coefficient k for a perfect solute mixing in the liquid phase (in the case of dilute Bi in Sn, $k = 0.26$). The effective partition ratio is assumed constant during

solidification when the solidification parameters are unchanged. After some initial transient, the Scheil law, derived in the perfect mixing case, still applies when replacing k by k^* [5]

$$c_s(f_s) = k^* c_0 (1 - f_s)^{(k^* - 1)}. \quad (1)$$

The symbols c_s, f_s, c_0 denote the mean solute concentration in a solid cross section, the solidified fraction and the initial liquid composition, respectively. Even in an extreme case scenario of purely diffusive mass transfer, the length of the initial transient would not exceed 5 mm for the slowest growth velocity of 2.5 μm s^{-1}. Only a small portion of the 20 cm long samples has to be discarded. In each solidified sample, seven sections are cut out and sent for analysis by the ICP-AES (inductively coupled plasma atomic emission spectroscopy) method: more precisely, at each of the seven positions, two neighbouring 3 mm long samples are analyzed. The mean of both values is recorded, while their difference is characteristic of the measurement uncertainty. The result consists in seven values of c_s for seven different solidified fractions f_s and the measured mean composition of the remaining part of the sample after the directionally solidified part. We adjust k^* and c_i for the Scheil law (1) to best fit these experimental data, using a least square method (see example in Fig. 2). In this example, the directionally solidified length is 193 mm and the total initial liquid sample length is 330 mm. The circles denote the measured concentration values and the full-line curve corresponds to the best fit using a Scheil law (1).

This experimental determination of k^* is performed for several conditions. Our working parameters are the growth rate V_i, the magnetic field intensity B and the tilt angle α of the sample with respect to the horizontal. They act through three non dimensional numbers (see Section 3), namely the solidification Péclet number Pe, the Hartmann number Ha and the product of the Grashof number with the Schmidt Number Gr Sc, defined

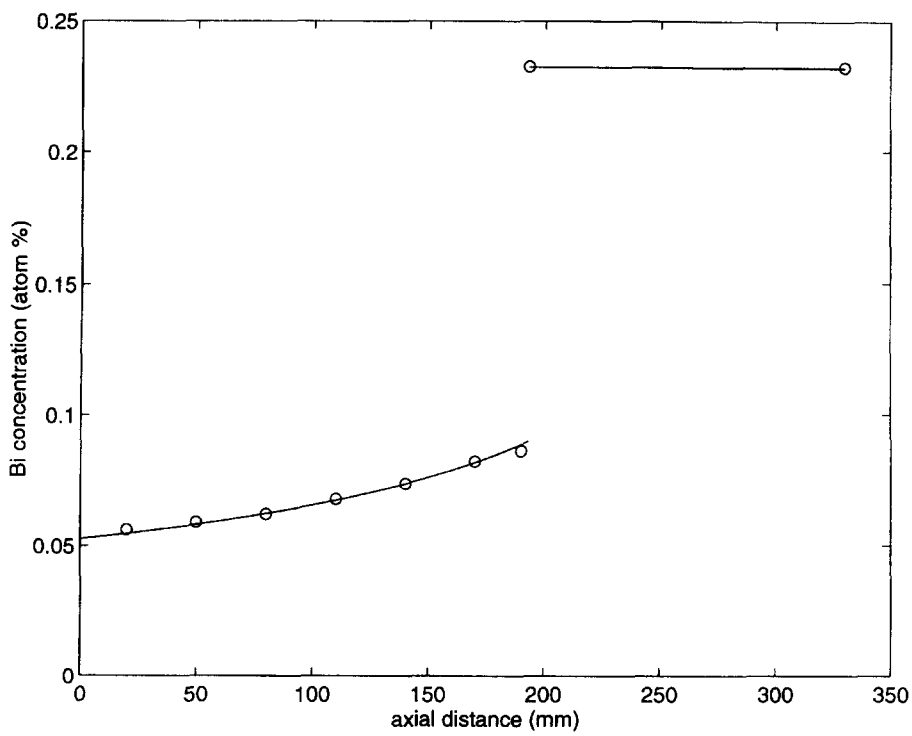

Fig. 2. Example of measured Composition data and fitting procedure for the case Gr Sc = 9.2×10^6, Pe = 23 and Ha = 66.

here as

$$\mathrm{Pe} = \frac{V_i H}{D}, \quad \mathrm{Ha} = \sqrt{\frac{\sigma}{\rho \nu}} BH, \quad \mathrm{Gr} = \frac{\beta g \cos\alpha \, G H^4}{\nu^2}, \quad \mathrm{Sc} = \frac{\nu}{D}, \tag{2}$$

where H, D, β, g, G, σ, ρ and ν denote the sample diameter (6 mm in our experiments), the solute diffusivity of Bi in liquid Sn, the thermal volume expansion coefficient of liquid tin, earth gravity, the axial thermal gradient (2400 K m^{-1} in our experiments), the electrical conductivity, density and kinematic viscosity of liquid tin (see Table 1 for the physico-chemical properties of dilute SnBi). The Schmidt number Sc only depends on the alloy. Its value, Sc = 200 indicates that solute diffusivity is small compared to kinematic viscosity, a very common feature of metals and semi-conductors. The Hartmann number, scaling the electromagnetic effects on the fluid motion in comparison with viscosity, reaches the maximum value 270 in our experiments when $B = 1.35$ T. In principle, one should also account for solutal buoyancy *via* a solutal Grashof number, but an analysis of the orders of magnitude presented in the next section shows that the thermal buoyancy effect is dominant.

Our results are summarized in Tables 2 and 3. In Table 2, the solidification Péclet number Pe is fixed to 23 (5 μm s^{-1} in our experiments) and three values of the product Gr Sc are investigated (corresponding to the tilt angles $\alpha = 15°$, 60° and 75°).

Table 1
Properties of liquid Sn–Bi dilute alloy. The solute diffusivity and equilibrium partition ratio result from the MEPHISTO space experiments [6]

Symbol	Description	value
T_m	Melting temperature	232°C
ρ	Density	7000 kg m^{-3}
β	Thermal expansion	1.06×10^{-4} K^{-1}
ν	Kinematic viscosity	2.6×10^{-7} m^2 s^{-1}
σ	Electrical conductivity	2.12×10^6 Ω^{-1} m^{-1}
α	Thermal diffusivity	2×10^{-5} m^2 s^{-1}
D	Solute (Bi) diffusivity	1.3×10^{-9} m^2 s^{-1}
κ	Equilibrium partition ratio	0.26

Table 2
Effective partition coefficient for Pe = 23

Gr Sc = 9.2×10^6		Gr Sc = 4.8×10^6		Gr Sc = 2.5×10^6	
Ha	k^*	Ha	k^*	Ha	k^*
		0	0.45	0	0.52
33	0.37	33	0.5		
66	0.39	66	0.44	66	0.69
135	0.41	135	0.5	135	0.79
270	0.44	270	0.56	270	0.82

Table 3
Effective partition coefficient for Gr Sc = 9.2×10^6

Pe = 11.5		Pe = 23		Pe = 46	
Ha	k^*	Ha	k^*	Ha	k^*
0	0.32			0	0.58
33	0.33	33	0.37		
66	0.3	66	0.39	66	0.59
135	0.31	135	0.41	135	0.7
270	0.35	270	0.44	270	0.72

Let us first indicate that, due to composition measurement uncertainty and to the least square method used, the estimated precision for these values of k^* is about ± 5% (see Ref. [7] for more details). As expected, it can be seen that the effective partition ratio increases either for increasing Péclet number or decreasing Gr Sc product (see, e.g., Ref. [8]). Moreover, it is here demonstrated a slight increase of this effective partition ratio with increasing the Hartmann number. If the braking electromagnetic effect is to reduce convection, one should not be surprised with this result. This effect is very small for Hartmann numbers up to 66 and more significant for the highest values (135 and 270). It also appears that the effect of the magnetic field occurs for a smaller Ha value in the case of the smallest Gr Sc product (see Table 2, Gr Sc $= 2.5 \times 10^6$). The values included in a box correspond to experiments for which growth interface destabilization occurred. After solidification, micrographs in a cross-section showed the so-called "poxes". This change in the solidification pattern is accompanied by a kind of "saturation" of the effective partition ratio with respect to the

Hartmann number (see Table 3, Pe = 46). Destabilized growth interfaces are out of the scope of this study, but we can conjecture that axial macrosegregation becomes less sensitive to convection in this regime.

3. Analysis of segregation

If solutal buoyancy can be neglected (the dilute alloy approximation will be discussed in the next paragraph), it is licit to determine first the liquid flow under the influence of thermal buoyancy and an axial magnetic field. The velocity field will then be used as an input in the segregation analysis.

3.1. Analysis of the buoyant MHD flow during solidification

The geometry and conditions for the flow are modeled as shown in Fig. 3. The cavity is a semi-infinite horizontal cylinder with an axial uniform temperature gradient and magnetic field. The magnetic field can safely be assumed undisturbed and we also expect inertial effects to play a negligible role. Indeed, our values for the Grashof number range from 1.24×10^4 to 4.62×10^4. In a cavity with a square cross-section and a length over height aspect ratio of four, Pratte and Hart [9] found experimentally a critical Grashof number of 2×10^5 for the onset of oscillations (they used mercury: Pr = 0.026). In the same configuration, Afrid and Zebib [10] found numerically a critical Grashof number equal to 1.25×10^5 (they assumed a zero Prandtl number). Below this critical value, the flow is steady and the effect of inertia essentially consists in tilting the recirculation loop. Under a magnetic field, the flow is efficiently damped and inertia becomes totally negligible (see Refs. [11, 12]). Using the Boussinesq approximation, two steady governing equations can be written for the divergence-free velocity and electric current density fields, $\boldsymbol{u}$ and $\boldsymbol{j}$ (see Ref. [13]), Ohm's law and the momentum equation:

$$\boldsymbol{j} = \sigma(-\nabla\varphi + \boldsymbol{u} \wedge \boldsymbol{B}), \tag{3}$$

$$\boldsymbol{0} = -\nabla p + \boldsymbol{j} \wedge \boldsymbol{B} - \rho\beta(T - T_0)\boldsymbol{g} - \rho\beta_c(c - c_0)\boldsymbol{g} + \rho\nu\Delta\boldsymbol{u}, \tag{4}$$

where φ and p denote the electric potential and pressure fields respectively, T the temperature field, T_0 a reference temperature (the growth interface temperature for instance), c the composition field, c_0 a reference composition (the initial liquid mean composition for instance) and β_c the solute expansion coefficient. Assuming, as checked in our experiments, a uniform temperature gradient, the relation $T - T_0 = Gz$ holds.

We now estimate the relative strength of thermal and solutal buoyancy forces in the absence of

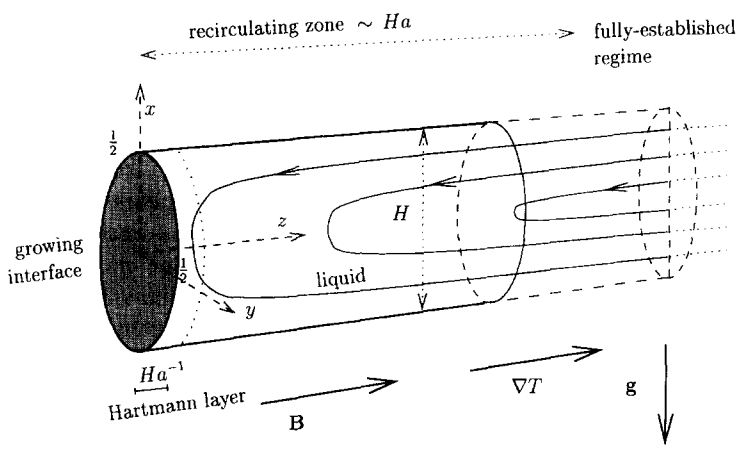

Fig. 3. Flow configuration.

magnetic field. Let us consider the effect of thermal buoyancy alone: the curl of the Navier–Stokes equation can be written,

$$\boldsymbol{0} = -\rho\beta\nabla T \wedge \boldsymbol{g} + \rho\nu\Delta(\mathrm{curl}\,\boldsymbol{u}). \tag{5}$$

The velocity varying over a length scale H, this equation provides us with the following magnitude order,

$$u_T \sim \beta g G\frac{H^3}{\nu}. \tag{6}$$

The same estimate can be found for the velocity induced by solutal buoyancy alone, H being replaced by d, the solute layer typical thickness,

$$u_c \sim \beta_c g \nabla c\frac{d^3}{\nu}. \tag{7}$$

Now, it is important to compare both velocity field at the same location, in the solute boundary layer. The estimate for u_c Eq. (7), satisfies to this condition but not that for u_T, which is estimated at the typical distance H from the growth interface; Eq. (6) must be multiplied by d/H. The ratio of this two contributions is,

$$\frac{u_c(d)}{u_T(d)} \sim \frac{\beta_c \nabla c\, d^2}{\beta G\, H^2}. \tag{8}$$

Anticipating on the analysis in Section 3, the composition gradient at the interface is $V_i/D(1-k)c_i$ from the solute rejection condition, where k, V_i and c_i denote the equilibrium coefficient, growth velocity and composition in the liquid at the interface. An upper bound of the boundary layer thickness d is D/V_i, for the purely diffusive case. Then Eq. (8) takes the form,

$$\frac{u_c(d)}{u_T(d)} \sim \frac{\beta_c(1-k)c_i D}{\beta G H^2 V_i}. \tag{9}$$

The solute expansion coefficient for SnBi is $\beta_c = 0.3$. For our smallest growth velocity $V_i = 5\ \mu\mathrm{m\ s}^{-1}$, and with a maximum 10^{-2}Bi mass composition (c_0/k in the diffusive case), the estimate of Eq. (9) leads to,

$$\frac{u_c(d)}{u_T(d)} \sim 5\times 10^{-2}.$$

It is licit to drop the solute buoyancy term in Eq. (4). Moreover, as our experiments are found to be far from the purely diffusive case, the contribution of solutal convection is smaller than suggested by the above estimate.

These governing Eqs. (3) and (4) are now written in a non dimensional form, using H, B, D/H, $D\sigma B/H$, DH and $\rho Dv/H^2$ as references for length, magnetic field, velocity, electric current density, electric potential and pressure:

$$\boldsymbol{j} = -\nabla\varphi + \boldsymbol{u}\wedge\boldsymbol{B} \tag{10}$$

$$\boldsymbol{0} = -\nabla p + \mathrm{Ha}^2\,\boldsymbol{j}\wedge\boldsymbol{B} + \mathrm{Gr\,Sc}\,z\boldsymbol{e}_x + \Delta\boldsymbol{u}, \tag{11}$$

where the same symbols have been used for non-dimensional variables. The non-dimensional parameters Gr Sc and Ha appear in these equations, while Pe is still hidden. The Péclet number Pe will intervene, when the growth rate will be considered: in our non-dimensional system, the pulling rate $-\mathrm{Pe}\,\boldsymbol{e}_z$ shall be added to the velocity field $\boldsymbol{u}$ in order to get the velocity field expressed in a coordinate system moving with the interface (see Section 3.2). In the following, only dimensionless quantities will be used.

From Eq. (10) and Eq. (11), a differential operator governing the velocity field can be derived, that helps finding the principal features of the buoyant flow. The curl operator has to be applied twice to Eq. (11) and once to Eq. (10). Direct substitution (see the detailed calculation in Ref. [14] or [15]) then leads to:

$$\mathrm{Ha}^2\frac{\partial^2\boldsymbol{u}}{\partial z^2} = \Delta^2\boldsymbol{u}. \tag{12}$$

Based on Eq. (12), three main regions (see Fig. 3) can be identified in the cavity:

- Hartmann layer: if a boundary layer develops near the solid-liquid interface, its thickness δ_{Ha} leads to the estimates $\partial^2/\partial z^2 \sim 1/\delta_{\mathrm{Ha}}^2$ and $\Delta^2 \sim 1/\delta_{\mathrm{Ha}}^4$. Eq. (12) leads then to the classical Hartmann boundary layer thickness (see Ref. [13]) $\delta_{\mathrm{Ha}} \sim \mathrm{Ha}^{-1}$.
- Recirculating zone: it is well known that Hartmann layers can not admit a significant flow rate [13], while it is obvious that far from the interface, a fully established parallel flow exists without influence of the magnetic field

($\boldsymbol{u} \wedge \boldsymbol{B} = \boldsymbol{0}$). If we look for a recirculating lengthscale L larger than the diameter (1 in our non-dimensional reference), the bi-Laplacian operator scales as 1 while the operator $\partial^2/\partial z^2$ scales as L^{-2}. Eq. (12) leads to $L \sim \mathrm{Ha}$.

- Fully established regime: from the above results, we can deduce that for $z \gg \mathrm{Ha}$, the expected fully established parallel flow exists.

Starting from this organization, the velocity magnitude order can be estimated in the different regions:

- Fully established regime: the flow is purely axial and viscous ($u_x = 0$ and scales as $u_z \sim \mathrm{Gr\,Sc}$, independent of Ha).
- Recirculating zone: by continuity, taking into account the relation $L \sim \mathrm{Ha}$, the vertical component of the velocity field scales as $u_x \sim \mathrm{Gr\,Sc/Ha}$ and the axial component as $u_z \sim (\mathrm{Gr\,Sc/Ha})z^2$.
- Hartmann layer: in this region the vertical component of the velocity reaches zero through the Ha^{-1} thickness, $u_x \sim \mathrm{Gr\,Sc}\ z$. Continuity on the Hartmann layer typical thickness then leads to $u_z \sim (\mathrm{Gr\,Sc/Ha})z^2$.

In order to obtain more precise informations on the velocity field, we now turn to a 2D model, which will also be used for segregation analysis (see Section 3.2). It is assumed that the features of the 3D flow are well described if the analysis is restricted to the vertical axial mid-plane $y = 0$. The cylindrical shape is replaced by the condition $\partial/\partial y = 0$. It can be proved (see Ref. [16]) that the electric potential is zero everywhere, such that Ohm's law takes a simplified form: $\boldsymbol{j}$ is purely directed along y and $j_y = -u_x$. The 2D equations have then been solved using a Fourier expansion analysis. The coefficients were calculated numerically so that boundary conditions are fulfilled ($\boldsymbol{u} = \boldsymbol{0}$). We shall not write here this exact 2D solution, which would require tedious and uninteresting calculations [15]. Suffice it to say that the above-mentioned features described for the 3D cylinder are present (Hartmann layer, recirculating region and fully- established regime). We also derived a simple approximate expression (a few percents departure from the exact solution), for high Hartmann numbers and in the vicinity of the solid-liquid interface, to be used in the order of magnitude analysis of the segregation problem (Section 3.2.2).

If the Hartmann layer is ignored, the velocity field approximates as:

$$u_z = \frac{8\mathrm{Gr\,Sc}}{9\mathrm{Ha}}(-zx + 4zx^3), \tag{13}$$

$$u_x = -\frac{\mathrm{Gr\,Sc}}{18\mathrm{Ha}}(1 - 8x^2 + 16x^4). \tag{14}$$

To take into account the Hartmann layer, the approximate velocity field has to be changed in (see Ref. [14]):

$$u_z = \frac{8\mathrm{Gr\,Sc}}{9\mathrm{Ha}}[-zx + 4zx^3] + \frac{8\mathrm{Gr\,Sc}}{9\mathrm{Ha}^2}[x - 4x^3](1 - \mathrm{e}^{-\mathrm{Ha}\,z}), \tag{15}$$

$$u_x = -\frac{\mathrm{Gr\,Sc}}{18\mathrm{Ha}}[1 - 8x^2 + 16x^4](1 - \mathrm{e}^{-\mathrm{Ha}\,z}). \tag{16}$$

3.2. Analysis of the axial segregation

3.2.1. Numerics

In the quasi-steady approximation, using c_∞ (the composition far from the interface, or mean liquid composition) as a reference for the concentration field, the equation governing concentration in the liquid takes the form:

$$\boldsymbol{u} \cdot \nabla c - \mathrm{Pe}\frac{\partial c}{\partial z} = \Delta c. \tag{17}$$

Moreover, the boundary conditions consist in a zero normal solute flux at the crucible boundaries ($\partial c/\partial n = 0$), $c = 1$ far from the solidification front and the solute rejection at the interface ($z = 0$):

$$c(1 - k)\mathrm{Pe} = -\frac{\partial c}{\partial z}. \tag{18}$$

It is well known that the solute concentration field forms a boundary layer near the interface and tends towards a uniform composition outside. We will only consider cases for which this solute layer is smaller than the sample diameter. This is the reason why we restricted the numerical calculations to the rectangle of aspect ratio 2 shown in Fig. 4. Nevertheless, the velocity field can not be considered as fully established at the distance 2 from the interface

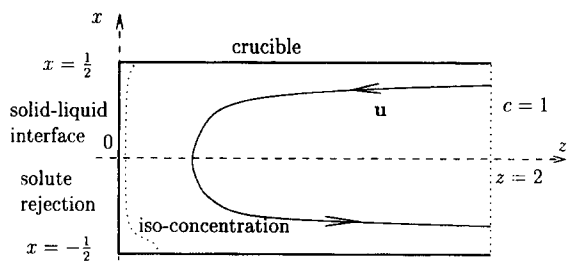

Fig. 4. 2D cavity, for numerical calculations.

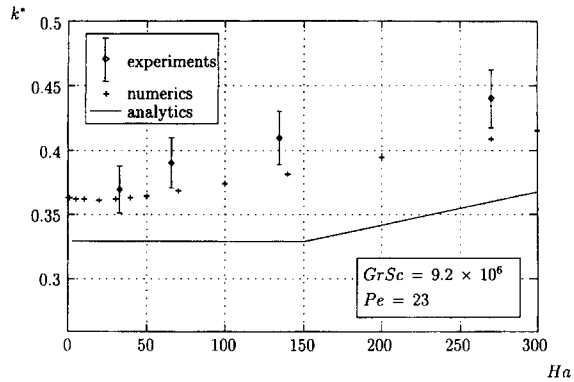

Fig. 5. Comparison between experimental numerical and analytical results.

and is calculated for a semi-infinite cavity. Indeed, the recirculating zone scales as Ha, and one should have such a Ha aspect ratio to get the fully established condition for velocity. For this reason, our exact Fourier series expansion solution proves necessary to determine the correct velocity field, if a reasonable geometry is adopted (it would be numerically difficult to increase the domain length for the velocity field while concentration forms a very thin boundary layer).

The FIDAP software (version 7.06), based on the finite elements method, was used for the calculations, performed on a HP 9000-735 working station. Rectangular, 9 nodes elements have been chosen with quadratic interpolation. The mesh contained 60 nodes in the axial direction and 50 in the transverse direction. The mesh was variable in space and concentrated near the walls. At the growing interface, the first node in the liquid is 1/1000 apart, which determines the smallest solute layer that can be modeled.

Each numerical calculation corresponds to a set of the non-dimensional numbers Gr Sc, Ha, Pe and k. The coefficients of the Fourier series expansion for the velocity field depend on Gr Sc and Ha only. Actually, they essentially depend on Ha, since they are merely proportional to Gr Sc. Then, for a given velocity field, the solute calculation (FIDAP) depends on Pe and k. From the derived concentration field, the effective partition ratio is determined as the product of k and of the mean concentration in the liquid at the growth interface. In Fig. 5, the experimental results are compared to the numerics for Gr Sc $= 9.2 \times 10^6$, $k = 0.26$ and Pe $= 23$. The calculated values are not identical to the measured ones, but the same tendency of slight increase of k^* with increasing Hartmann numbers is observed. A possible explanation of the discrepancy may be found in the 2D nature of the analysis. We observe from the numerical analysis that the mentioned increase does not start immediately when the Hartmann number becomes larger than one. Indeed, a slight decrease is first observed, and k^* is smaller in the range $0 \leqslant \mathrm{Ha} \leqslant 40$ than without magnetic field.

3.2.2. *Order of magnitude analysis*

The order of magnitude analysis is based on the estimate of the solute layer thickness attached to the growing interface. Wilson [17] proved that the effective partition ratio is uniquely determined by the knowledge of the solute layer thickness, provided this thickness is defined as follows. Let us denote $\tilde{c}_0$ the mean solute concentration in the liquid near the interface and $\mathrm{d}\tilde{c}/\mathrm{d}z$ the mean axial solute gradient at the interface. The non dimensional solute layer thickness δ is defined as $(\tilde{c}_0 - 1)/ - \mathrm{d}\tilde{c}/\mathrm{d}z$. The relation between k^* and δ is [17]:

$$k^* = \frac{k}{1 - (1 - k)\,\mathrm{Pe}\,\delta}. \tag{19}$$

If δ can be estimated, Eq. (19) then allows us to estimate k*.

The derivation of the solute boundary layer thickness in Czochralski growth was first proposed

by Burton et al. [5] in 1953. Their work was later extended to other solidification configurations, and it was shown that δ could always be estimated when the velocity field in the vicinity of the interface is known (see e.g. Ref. [8] and references there). Denoting $\tilde{u}_z(z)$ the mean velocity field along the upper part of the cavity (here $0 < x < \frac{1}{2}$, the following general equation derived from an order of magnitude analysis of Eq. (17) when $\delta \ll 1$:

$$\tilde{u}_z(\delta) + \mathrm{Pe} = 1/\delta. \tag{20}$$

For small values of the velocity field, the equation leads to $\delta = \mathrm{Pe}^{-1}$, which corresponds exactly to the solution for purely diffusive transport conditions. Conversely, we focus here only on the convective case, when Pe can be neglected in Eq. (20). This approximation allows us to highlight the trends of the influence of the magnetic field. The equation to solve is:

$$\tilde{u}_z(\delta) = 1/\delta. \tag{21}$$

The approximate velocity field given by Eqs. (15) and (16) will be used. Two asymptotic cases can be distinguished: the case when the Hartmann layer is much thinner than δ and the case when it is much larger than δ. In the first case, Eqs. (13) and (14) can be used while, in the second, the $1 - \mathrm{e}^{-\mathrm{Ha}\, z}$ factor is linearized in Eqs. (15) and (16). It is easy to derive $\tilde{u}_z$ and the corresponding solution δ of Eq. (21):

$$\delta < \mathrm{Ha}^{-1} \Rightarrow \tilde{u}_z(z) = -\frac{\mathrm{Gr\,Sc}}{18} z^2$$

$$\Rightarrow \delta = 2.6(\mathrm{Gr\,Sc})^{-1/3}, \tag{22}$$

$$\delta > \mathrm{Ha}^{-1} \Rightarrow \tilde{u}_z(z) = -\frac{\mathrm{Gr\,Sc}}{9\mathrm{Ha}} z$$

$$\Rightarrow \delta = 3(\mathrm{Gr\,Sc})^{-1/2}\mathrm{Ha}^{1/2}. \tag{23}$$

Going back to the conditions $\delta < \mathrm{Ha}^{-1}$ or $\delta > \mathrm{Ha}^{-1}$, the limit between these two asymptotic cases is found, $\mathrm{Ha} \sim (\mathrm{Gr\,Sc})^{1/3}$. For Ha below (resp. above) this value, Eq. (22) holds (resp. Eq. (23)). This relation $\mathrm{Ha} \sim (\mathrm{Gr\,Sc})^{1/3}$ defines a "threshold value" for the magnetic field to become efficient. A smaller magnetic field has no effect on segregation, even though convection may already be significantly damped, and a higher magnetic field tends to decrease axial segregation. Even in the active regime, the effect of the magnetic field is moderate regarding to the square root dependence on the Hartmann number in Eq. (23).

A physical approach of this result can be outlined. The inactive regime is characterized by the fact that the solute boundary layer is smaller than the Hartmann layer. Indeed, at the scale of the solute layer, the velocity field is insensitive to the magnetic field, since the far velocity scales as Ha^{-1} while the Hartmann thickness also scales as Ha^{-1}. Conversely, when the solute layer is larger than the Hartmann layer, mass transport becomes sensitive to the Ha^{-1} decrease of the velocity field.

The above result is drawn in Fig. 5 in full line: the results were derived in terms of k^* using Eq. (19). The discrepancy with numerics and experiments can be explained both by the approximate nature of the order of magnitude analysis and by the neglected Pe number in Eq. (20). Nevertheless, the tendencies compare well. We tried then to check the validity of the order of magnitude analysis, when the convective regime (negligible Pe in Eq. (20)) is well achieved. In Fig. 6, numerical and order of magnitude results (OMA) for δ are compared for a small Péclet number $\mathrm{Pe} = 1$. Two different Gr Sc numbers were investigated, giving opportunity to detect the variation of the threshold $\mathrm{Ha} \sim (\mathrm{Gr\,Sc})^{1/3}$. The Ha number range was enlarged up to $\mathrm{Ha} = 1000$, to improve the comparison. In this Fig. 6, the multiplication factors in Eqs. (22) and (23) have been changed to 4.3 and 4.2, respectively (instead of 2.6 and 3), to best fit the numerical values. In other words, the magnitude order analysis (before modification) and numerical results differ by about 40%: it is a usual feature of an order of magnitude analysis to predict essentially power laws, which are independent of any multiplication by a constant factor. Moreover, the use of the new factors provides an excellent quantitative agreement between OMA and numerical results for the solute boundary thickness. To finish with these multiplication factors, it should be underlined that they are the same for both cases $\mathrm{Gr\,Sc} = 10^6$ and $\mathrm{Gr\,Sc} = 10^8$ and fit equally the two curves. The numerical prediction of the threshold value also seems to obey the relation $\mathrm{Ha} \sim (\mathrm{Gr\,Sc})^{1/3}$.

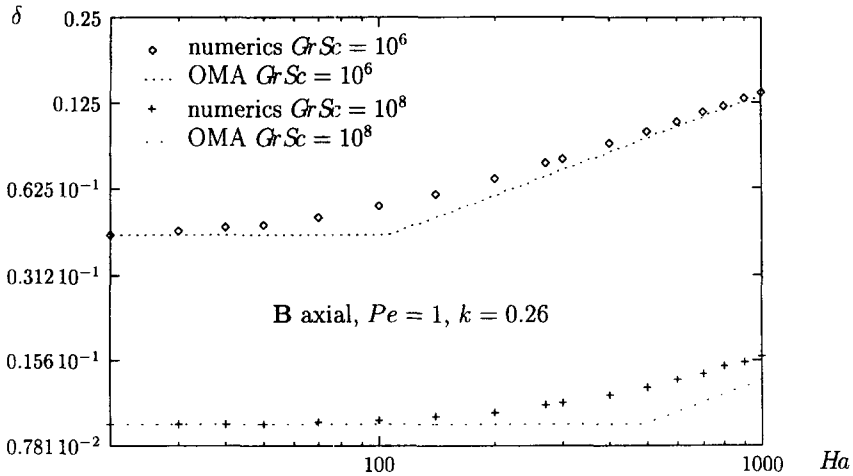

Fig. 6. Comparison between numerical and analytical results.

4. Conclusions

A moderate effect on axial solute segregation has been experimentally demonstrated for tin–bismuth alloys solidified in the presence of an axial magnetic field. The velocity field in the melt has been analyzed in the framework of a 2D model including the braking effect of the magnetic field. This velocity field has been included in a numerical 2D model for concentration and effective partition ratios k*, depending on the applied magnetic field magnitude, have been derived. In parallel, using again this velocity field, an order of magnitude analysis of the solute transport equation has led us to an estimate for the solute boundary layer thickness. This thickness and the effective partition ratio k* being in unique correspondence, order of magnitude analysis and numerical results have been compared, with fair agreement with experimental values. Moreover, the order of magnitude analysis has revealed two distinct regimes for the magnetic field influence. The thickness δ is found to scale as $(\mathrm{Gr\,Sc})^{-1/3}$ when $\mathrm{Ha} \ll (\mathrm{Gr\,Sc})^{1/3}$ and as $(\mathrm{Gr\,Sc})^{-1/2}\mathrm{Ha}^{1/2}$ when $\mathrm{Ha} \gg (\mathrm{Gr\,Sc})^{1/3}$. An axial magnetic field thus has to be strong enough before it can have an impact on axial segregation.

The method of segregation analysis under magnetic field developed in this paper can be extended to other aspects. Radial segregation, the case of a transverse vertical magnetic field and also the vertical Bridgman configuration with axial magnetic field [15, 7] have already been investigated. More generally, as soon as an expression for the velocity field is available, these analyses (numerical and in terms of magnitude orders) can be followed. For instance, analytical expressions for the flow in Czochralski growth configurations have been obtained (see, e.g., Ref. [18] and references there).

To conclude, some ideas deserve to be highlighted. As already reported [8], only the velocity field within the solute boundary layer controls its thickness: in the regime $1 \ll \mathrm{Ha} \ll (\mathrm{Gr\,Sc})^{1/3}$, the average velocity field intensity decreases with increasing values of Ha, while its value at the solute layer scale remains unchanged, meaning that there will be no effect of the magnetic field. It is also important to insist again on the benefits gained with the order of magnitude analysis. Estimates of the effective partition coefficient and of its dependence with respect to the magnetic field intensity are derived in terms of concise equations that can be easily used by a practician to account for his own growth conditions.

Acknowledgements

The present work was conducted within the framework of the GRAMME agreement between the CNES and the CEA.

References

[1] D.T.J. Hurle, E. Jakeman, C.P. Johnson, J. Fluid Mech. 64 (1974) 565.
[2] C. Vives, C. Perry, Int. J. Heat Mass Transfer 30 (1987) 479.
[3] D.H. Matthiesen, M.J. Wargo, S. Motakef, D.J. Carlson, J.S. Nakos, A.F. Witt, J. Crystal Growth 85 (1987) 557.
[4] M.C. Flemings, Solidification Processing, McGraw-Hill, New York, 1974.
[5] J.A. Burton, R.C. Prim, W.P. Slichter, J. Chem. Phys. 21 (11) (1953) 1987.
[6] J.J. Favier, P. Lehmann, J.J. Garandet, B. Drevet, H. Herbillon, Acta Mater. 44 (12) (1996) 4899.
[7] A.C. Neubrand, PhD Dissertation, INPG, Grenoble, CENG/DEM/SES, 1995.
[8] J.P. Garandet, J.J. Favier, D. Camel, in: D.T.J. Hurle (Ed.), Handbook of Crystal Growth, vol. 2, North-Holland, Amsterdam, 1994 Ch. 12.
[9] J.M. Pratte, J.E. Hart, J. Crystal Growth 102 (1990) 54.
[10] M. Afrid, A. Zebib, Phys. Fluids A 2 (8) (1990) 1318.
[11] H. Ben Hadid, D. Henry, S. Kaddeche, J. Fluid Mech. 333 (1997) 23.
[12] H. Ben Hadid, D. Henry, J. Fluid Mech. 333 (1997) 57.
[13] R. Moreau, Magnetohydrodynamics, Kluwer, Dordrecht, 1990.
[14] T. Alboussière, J.P. Garandet, R. Moreau, J. Fluid Mech. 253 (1993) 545.
[15] T. Alboussière, PhD Dissertation, INPG, Grenoble, CENG/DEM/SES, 1994.
[16] J.P. Garandet, T. Alboussière, R. Moreau, Int. J. Heat Mass Transfer 35 (4) (1992) 741.
[17] L.O. Wilson, J. Crystal Growth 44 (1978) 247.
[18] L.N. Hjellming, P.A. Tolley, J.S. Walker, J. Fluid Mech. 249 (1993) 1.